optica

Waveguide-integrated three-dimensional quasi-phase-matching structures

Jörg Imbrock,* Lukas Wesemann, ● Sebastian Kroesen, Mousa Ayoub, ● and Cornelia Denz

Institute of Applied Physics and Center for Nonlinear Science, University of Münster, Corrensstr. 2, 48149 Münster, Germany
*Corresponding author: imbrock@uni-muenster.de

Nonlinear photonic structures with a modulated second-order nonlinearity are used widely for quasi-phase-matched parametric processes. Creating three-dimensional (3D) nonlinear photonic structures is promising but still challenging, since standard poling methods are limited to two-dimensional structures. Light-induced quasi-phase matching (QPM) can overcome this issue by a depletion of the second-order nonlinearity with focused femtosecond laser pulses. We report, to the best of our knowledge, the first integration of a 3D QPM structure in the core of a lithium niobate waveguide applying light-induced fabrication. Depressed-cladding waveguides and embedded QPM structures are fabricated by femtosecond laser lithography. The 3D capability is exploited by splitting the QPM gratings in the waveguide core into two or four parts, respectively. These monolithic nonlinear waveguides feature parallel multi-wavelength frequency conversion. Finally, we demonstrate a concept for second-harmonic beam shaping taking advantage of a helically twisted nonlinear structure. Our results open new avenues for creating highly efficient advanced QPM devices.

1. INTRODUCTION

Quasi-phase matching (QPM) is used in nonlinear optics for high-efficiency frequency conversion such as difference-frequency generation, sum-frequency generation, and second-harmonic generation (SHG), respectively [1,2]. Applications include single-frequency sources, broadband parametric processes, cascaded second-order interactions, and quantum optical devices [3–6]. Lithium niobate (LiNbO$_3$) is one of the most important crystals for photonic applications due to its high nonlinear optical and electro-optical coefficients. QPM can be realized in LiNbO$_3$ by periodic poling, i.e., inverting the direction of spontaneous polarization by applying an external electric field by patterned electrodes [7]. The modulation of the second-order nonlinearity between $+\chi^{(2)}$ and $-\chi^{(2)}$ allows for the realization of a variety of periodic, quasi-periodic, and also random nonlinear photonic structures [8–11]. However, electric field poling is limited to structure sizes of some micrometers and to 2D structures. 3D nonlinear photonic crystals could enable many new schemes of manipulation and control of nonlinear optical interactions such as simultaneous QPM of different nonlinear processes, volume nonlinear holography, and nonlinear beam shaping. To overcome the limitations of 2D nonlinear photonic structures, focused infrared femtosecond laser pulses have been applied to modulate the $\chi^{(2)}$ nonlinearity. Known principles are all-optical local domain inversion [12,13], local depletion of the nonlinearity [14], and pyroelectric field-assisted

local domain inversion [15]. While the latter one can produce large 1D and 2D nonlinear photonic structures with high resolution, the two former ones are applicable for 3D structures. Recently, 3D nonlinear photonic crystals have been experimentally demonstrated using focused femtosecond laser pulses [16–18]. However, these structures are small in size and therefore low in efficiency. Higher efficiencies can be achieved by increasing the length of the nonlinear photonic crystal [19] or by embedding QPM structures into waveguides [20]. While fs laser lithography has been used to write waveguides into periodically poled LiNbO$_3$ [21–26], Kroesen et al. have fabricated efficient single-period quasi-phase-matched waveguides by structuring the $\chi^{(2)}$ nonlinearity in 1D using light-induced QPM (LiQPM) [27].

In this paper, we report the integration of 2D and 3D nonlinear structures in the core of a lithium niobate waveguide for efficient advanced QPM schemes. Depressed-cladding waveguides and embedded LiQPM structures are fabricated by femtosecond laser lithography (Fig. 1). First, we optimize the writing parameters for single-mode guiding and high conversion efficiency. Then, we demonstrate broadband SHG in a chirped grating and multi-wavelength SHG in two sequential gratings. Furthermore, we extend LiQPM to three dimensions by splitting the QPM gratings in the waveguide core into two and four parts, respectively. Finally, we propose a concept for the nonlinear generation of optical vortex beams by a helically twisted nonlinear susceptibility. Helically periodically poled crystals have been suggested for the
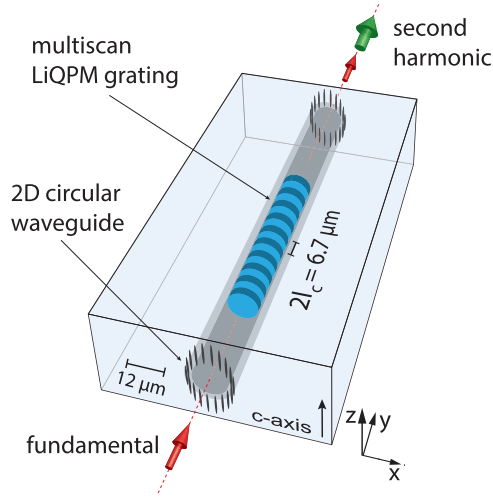
Fig. 1.   Schematic design of a LiQPM waveguide that consists of a multiscan $\chi^{(2)}$ grating and a circular type-II waveguide fabricated in a single inscription sequence.

generation of SH vortices and optical vortex converters [28,29]. However, such 3D structures cannot be produced by traditional electric field poling. Up to now, the experimental demonstration of nonlinear vortex generation from fundamental waves that do not carry angular optical momentum (OAM) was limited to 2D transverse geometries [30–33]. We show that this limit can be lifted by LiQPM.

2. PRINCIPLE OF LIGHT-INDUCED QUASI-PHASE MATCHING

Under collinear phase matching, the change in the amplitudes A_ω and $A_{2\omega}$ of a fundamental wave and SH propagating along the y axis of the crystal (Fig. 1), respectively, are described by the following two coupled-mode equations [22]:
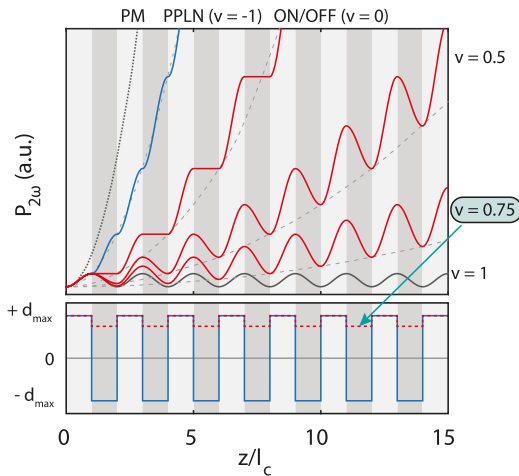

Fig. 2.   Calculated SH build-up inside the nonlinear material assuming phase matching (PM) and QPM by PPLN and LiQPM structures where the second-order nonlinearity is periodically damped to a certain degree instead of domain inversion. The dashed lines are the analytical solutions of the second-harmonic power in the undepleted pump regime of the form $P_{2\omega} \propto d_{\text{eff}}^2 z^2$, with the respective nonlinear coefficient d_{eff}.
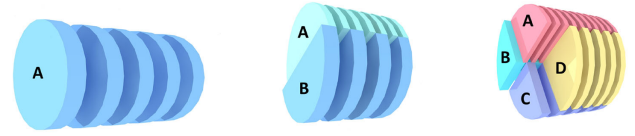

Fig. 3.   Three schemes to modulate the $\chi^{(2)}$ nonlinearity inside the waveguide core for QPM. One period (A), two periods (A, B), and four periods (A, B, C, D). For SHG of 1064 nm, the core diameter is typically 12 μm, and the period of the QPM grating is approximately 6.6 μm (cfg. Fig. 1).

$$\frac{d}{dy}A_\omega = -i\kappa^* d(\mathbf{r}) A_\omega^* A_{2\omega} \exp(-i\Delta ky) - \alpha_\omega A_\omega, \quad (1)$$

$$\frac{d}{dy}A_{2\omega} = -i\kappa d(\mathbf{r}) A_\omega^2 \exp(i\Delta ky) - \alpha_{2\omega} A_{2\omega}, \quad (2)$$

$$\kappa^2 = \frac{2\omega^2}{\epsilon_0 c^3} \frac{1}{n_\omega^2 n_{2\omega} S_{\text{eff}}}, \quad (3)$$

with the phase mismatch

$$\Delta k = k_{2\omega} - 2k_\omega, \quad (4)$$

and S_{eff} being the cross section of the overlap of the fundamental and SH mode. The absorption coefficients α_ω and $\alpha_{2\omega}$ of the fundamental and SH, respectively, account for the losses in the waveguide as well as in the QPM gratings. The amplitudes A_ω and $A_{2\omega}$ of the fundamental and SH are normalized such that $|A_i|^2 = P_i$, with P_i representing the respective power. The nonlinear coefficient $d(\mathbf{r})$ can be in general modulated in any direction using LiQPM. For 1D QPM, the nonlinear coefficient is modulated only along the y axis $d(y) = d_{\text{max}}g(y)$. The normalized rectangular function $g(y)$ incorporates the period $\Lambda = 2l_c = 2\pi/\Delta k$ to compensate for the phase mismatch, with the coherence length l_c. The largest nonlinear coefficient in LiNbO$_3$ is $d_{\text{max}} = d_{33}$ for an ee-e process. A Fourier transform of $d(y)$ yields an effective nonlinear coefficient:

$$d_{\text{eff}} = \frac{d_{\text{max}}}{\pi}(1 - v), \quad (5)$$

with the visibility $v = d_{\text{min}}/d_{\text{max}}$. Thus, a periodically poled structure with $d_{\text{min}} = -d_{\text{max}}$ has the largest effective nonlinearity $d_{\text{eff}} = 2/\pi \, d_{\text{max}}$, as can be seen in Fig. 2. However, a damping of the nonlinearity by LiQPM is already sufficient for effective QPM.

We can realize a 3D modulation of the nonlinearity if we, for instance, split the waveguide core into two or four sections while each section is individually modulated, as shown in Fig. 3. We use this approach for SHG of multiple fundamental frequencies. We can also express the nonlinear coefficient in polar coordinates $d(\mathbf{r}, \theta)$. If we modulate the rectangular function $g(\mathbf{r}, \theta)$ in addition transversely with the phase $2\pi/\Lambda z + l\theta$, we will generate a SH vortex of charge l for first-order QPM [28].

3. METHODS

A. Writing Waveguides and 3D Nonlinear Structures with fs Laser Pulses

A schematic of the layout is depicted in Fig. 1. The proposed design consists of a circular waveguide and an embedded multiscan LiQPM grating of damped nonlinearity for the SHG process. We

use undoped congruent LiNbO$_3$ samples cut from a *z*-cut wafer with the dimensions $12 \times 10 \times 0.5$ mm^3. The *z* and *y* surfaces are polished to optical quality. The waveguides and nonlinear structures are directly written into the crystals using a fs laser lithography setup [34]. The system consists of a regenerative Ti:sapphire amplifier operating at a central wavelength of 800 nm with a repetition rate of 1 kHz (Coherent Legend). The pulse duration is 110 fs, and the maximum pulse energy is 1 mJ. The beam is attenuated by neutral density filters followed by a motorized half-wave plate in combination with a polarizing beam splitter. The laser output is triggered synchronous to the position of the stage, which is crucial for the inscription of transverse grating structures. The beam is subsequently focused into the lithium niobate sample using a microscope objective with a numerical aperture (NA) of 0.8. All structures are inscribed with a writing beam linearly polarized along the *y* axis and parallel to direction of the waveguides. The sample is placed on a computer-controlled Aerotech motion stage and thereby translated in three dimensions with nanometer precision relative to the focus of the laser beam. The multiscan LiQPM gratings are inscribed with 80 µm/s translation velocity. The transverse feature size along the *x* and *y* axes of the QPM grating is approximately 300 nm, and the feature size along the optical *z* axis is 700 nm. We can achieve with this setup in periods down to 700 nm [34] enabling SHG into the ultraviolet spectral region. The pulse energies to write the waveguides range between 120 nJ and 200 nJ, while the core is modulated with lower pulse energies between 60 nJ and 90 nJ.

B. Measurement of the Linear and Nonlinear Properties

A setup with two continuous-wave lasers at 1059 nm (Sacher Lasertechnik DFB laser diode) and 532 nm (Coherent Compass 315M) is used in order to linearly characterize the fabricated waveguides regarding their insertion losses and mode profiles. The output of both lasers is coupled into single-mode fibers and guided to the lithium niobate sample. The near-field output of the waveguides is afterwards imaged onto a camera by a 20× microscope objective with an NA of 0.4, which allows screening the mode profile at the exit facet.

We use a laser-scanning SHG microscope to image the fs laser-induced structures in 3D [35,36]. The fundamental beam of a Ti-Sapphire laser (800 nm, 80 MHz repetition rate, about 60 fs pulse duration, and up to 3.5 nJ pulse energy) is coupled to a commercial laser-scanning microscope (Nikon eclipse, Ti-U) and tightly focused by the microscope objective with an NA of 0.8 to a near-diffraction-limited spot in the sample. The position of the focus is raster-scanned in the xy plane by a piezoelectric table (P-545, PI nano). The intensity of the SH signal is collected by a condenser lens (NA 0.9) and measured by a photomultiplier as a function of the focus position.

Quasi-phase-matched SHG is performed with a *Q*-switched Nd:YAG laser with a wavelength of 1064 nm, pulse duration of 4.1 ns, and repetition rate of 100 Hz. Fabricated devices are mounted on a controllable heating element with a resolution and temperature stability of 0.1°C. The fundamental wave is extraordinarily polarized and coupled into the waveguides using a 4× microscope objective with NA = 0.1. The back-facet is imaged onto a camera by a 20× microscope objective. Typical pulse energies are on the order of a few µJ, and the maximum fundamental peak power used is 400 W.

4. RESULTS AND DISCUSSION

A. Influence of the Writing Pulse Energy

Efficient LiQPM waveguide devices should exhibit single-mode guiding and low losses at the fundamental frequency and SH, respectively, as well as a high nonlinearity. Therefore, in a first step, the insertion losses and mode profiles have been measured in dependence on the writing energy between 120 nJ and 200 nJ and as a function of the core diameter between 10 µm and 25 µm. A good trade-off between low losses and single-mode guiding is achieved with a core diameter of 12 µm at an energy of 150 nJ. These waveguides exhibit reasonable low insertion losses of 8.6 dB at 532 nm and only weakly multimode profiles as well as very symmetric profiles at 1059 nm accompanied by low insertion losses of 5.5 dB. Larger-core diameters support multimode guiding, while a smaller-core diameter leads to increased insertion losses.

A total number of 17 individual devices with a 5 mm long LiQPM grating are fabricated using a 10.2 mm long sample. The LiQPM gratings are adjusted precisely in the middle of the waveguide core, as can be seen in Fig. 4. The performed analysis of SH power and insertion losses covers the full range from no visible detectable modification in the LiQPM grating to strong laser-induced damage. All temperature tuning curves are evaluated under the same conditions, and the characteristic build-up of the normalized SH power as a function of the writing pulse energy is indicated by the gray shaded area in Fig. 5. The presented data follow an almost linear slope that rapidly drops down when a certain energy threshold value around 80 nJ is exceeded. This
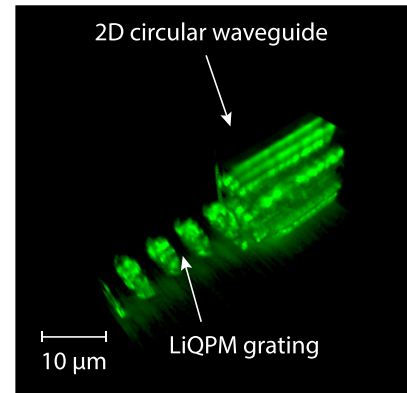

Fig. 4. Laser-scanning SHG microscope image of waveguide and LiQPM grating with a period of $\Lambda = 6.6$ µm. The first part of the grating is not surrounded by a waveguide in this example to illustrate that the grating is located in the middle of the waveguide.
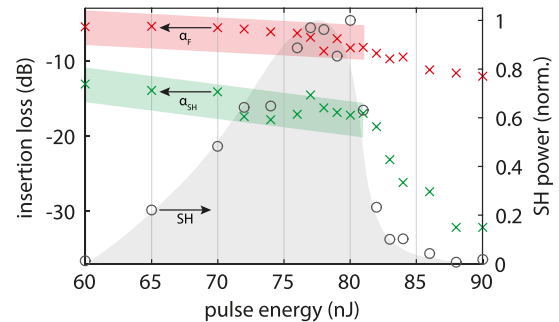

Fig. 5. Power of the SH and insertion losses at both wavelengths measured in dependence on the writing pulse energy.

behavior is associated with a significant increase in insertion losses at both wavelengths. Particularly, the power attenuation of the SH wave is subject to a steep change, and extremely high values of more than -30 dB are obtained, although the grating length is 5 mm only. Considering the associated propagation losses, the $\chi^{(2)}$ modulation saturates for high-pulse energies. The optimum energy regime between 75 nJ and 80 nJ that is employed to obtain a localized damping of the $\chi^{(2)}$ nonlinearity is associated with severe material damage and high optical attenuation, as can be seen in Fig. 5 and related optical microscope images. This energy regime can be clearly identified with a starting type-II filamentation process. This is also reflected in the fact that LiQPM gratings do not show any signature of reversibility or reduction in efficiency upon thermal treatment.

B. Chirped and Single-Period QPM Grating

Chirped gratings can be used for the compression and shaping of ultrashort laser pulses [37–39]. Figure 6 shows the experimental temperature tuning and mode images of a chirped LiQPM device in comparison to a single-period device fabricated with equal parameters. Both gratings are 7 mm long and integrated into a 9.7 mm long waveguide. The single-period grating has a period of 6.6 µm, while the chirped grating has a period linearly increasing from $\Lambda_{\text{start}} = 6.586$ µm to $\Lambda_{\text{end}} = 6.614$ µm. The chirp leads to an almost ideal top-hat profile and a significantly increased temperature acceptance width of approximately 11.3°C. This corresponds to an equivalent absolute increase in the spectral bandwidth from 200 pm to 0.94 nm. The integrals of the unchirped and chirped tuning curves are 77 W°C and 152 W°C, respectively. This is not in contradiction to Plancherel's theorem because the fundamental power of 291 W already exceeds the undepleted pump regime for the single-period grating [27], while the efficiency of the chirped grating is still linearly increasing with increasing pump power. It should be noted that the phase-matching temperature shifts by approximately -30°C with respect to the dispersion of congruent LiNbO$_3$ [40]. This shift corresponds to a change in the bulk material's dispersion of $|n_{2\omega} - n_\omega| = 5.5 \times 10^{-4}$ due to the refractive index profile of the waveguide [27]. However, the additional refractive index change in the periodic $\chi^{(2)}$ grating is small and does not influence the phases of the fundamental and SH waves much.
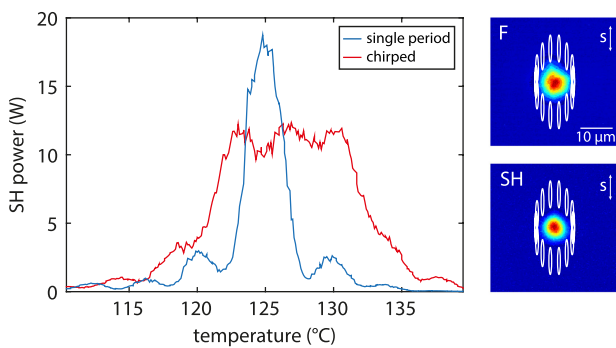
C. Split-Core Structures for Multiple QPM

LiQPM waveguide devices can be customized to allow for cascaded frequency conversion processes and parallel multi-wavelength SHG. The proposed LiQPM fabrication method based on direct laser writing allows monolithic inscription of such devices, as shown in Fig. 7. As indicated in the associated schematic, two separated LiQPM gratings with periods of 6.6 µm and 6.525 µm are inscribed into a 9.8 mm long waveguide. Hence, the temperature tuning curve shows two distinct maxima at 124.7°C and 167.9°C with an average SH power of 6.7 W at 291 W fundamental power. The two gray lines are numerical calculations by integrating Eqs. (1) and (2) taking into account different absorption coefficients of the gratings $\alpha_\omega^{\text{grating}} = 6.7$ dB/cm and $\alpha_{2\omega}^{\text{grating}} = 17.2$ dB/cm, and of the waveguides $\alpha_\omega^{\text{waveguide}} = 4.6$ dB/cm and $\alpha_{2\omega}^{\text{waveguide}} = 7.7$ dB/cm for the fundamental and SH waves, respectively. As the fundamental wave propagates first through the grating with the shorter period and higher phase-matching temperature, this efficiency is larger than that of the second grating. This is in accordance with our numerical calculations. The temperature acceptance width of 6.8°C is in good agreement with the performed numerical calculation and the comparably short grating length of 3.5 mm. Since such a device is typically designed for simultaneous multi-wavelength operation rather than SHG of a single fundamental wave at different temperatures, the notation multi-wavelength LiQPM is used here. Assuming an operation temperature of 125°C, the presented LiQPM waveguide device allows for simultaneous SHG of 1064 nm and 1060.5 nm radiation. The employed periods and associated phase-matching wavelengths are selected here in a narrow region according to the 1064 nm laser source used for the nonlinear probe experiments. In general, fabrication of such a device can be on-the-fly adapted to any design wavelength. Furthermore, an arbitrary succession of LiQPM gratings is possible.

A novel approach that allows for parallel instead of sequential multi-wavelength SHG is shown in Fig. 8. In this configuration, the LiQPM grating inside the waveguide core is split into two segments, each of which has its own period and associated design wavelength as indicated in the schematic (cf. Fig. 3). The obtained SH power of the split-core LiQPM device is similar to the former sequential configuration (Fig. 7), and an average efficiency of

Fig. 6. Experimental temperature tuning of a chirped LiQPM device for broadband SHG at 291 W fundamental power in comparison to a single-period device fabricated with equal parameters. Right: images of the fundamental and chirped second-harmonic mode at the end of the waveguide.
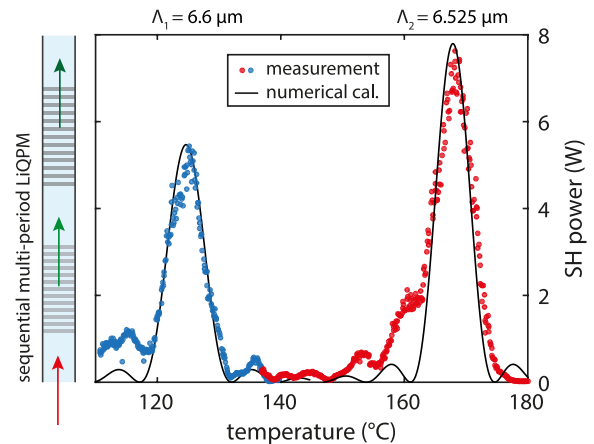

Fig. 7. Sequential multi-wavelength SHG. The sequential scheme is composed of two successive LiQPM gratings inscribed into a single waveguide.
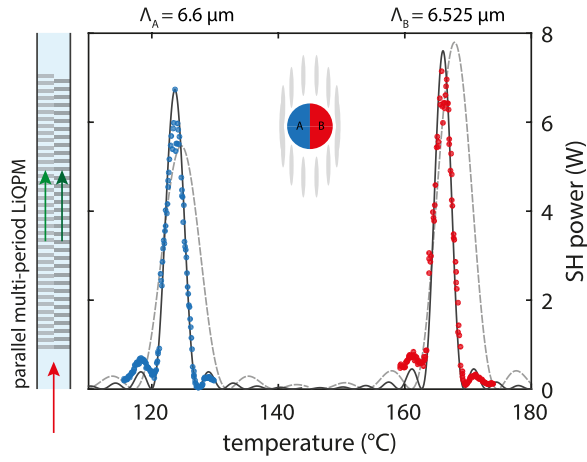
Fig. 8. Parallel multi-wavelength SHG. Parallel waveguide SHG is realized in a novel split-core approach as illustrated in the schematic.

Fig. 9. Split-core LiQPM device for multi-wavelength SHG. A three-dimensional LiQPM grating composed of four segments is inscribed into the waveguide core to enable simultaneous frequency conversion of four individual design wavelengths.

2.4% is achieved at 291 W fundamental power. The temperature acceptance width of 3.25°C is in good agreement with the 7 mm long grating fabricated with 84 nJ, as indicated by the numerical calculation. To allow direct comparison, the numerical traces of the sequential gratings (Fig. 7) are shown again by the gray dashed lines. In this configuration, the reduced overlap between a LiQPM segment and the fundamental wave, which lowers the SHG efficiency, is almost exactly compensated for by the increased grating length. This is also reflected in the numerical calculation where doubling of the effective area from 75 μm^2 to 150 μm^2 is assumed.

As a next step towards complex nonlinear devices, the number of LiQPM segments is increased, which allows for parallel multi-wavelength SHG of four individual wavelengths, as shown in Fig. 9. Fabrication parameters such as grating length and pulse energy are adopted from the previous configuration to allow direct comparison. All four distinct SHG maxima are observed at the predefined phase-matching temperatures, which clearly demonstrates the functionality of the fabricated 3D LiQPM device. According to the periods of 6.625, 6.6, 6.55, and 6.525 μm, simultaneously quasi-phase-matched SHG of 1065.3, 1064, 1061.6, and 1060.5 nm radiation is possible by this unique approach. An average SH power of 1.33 W is achieved, which corresponds to an efficiency of 0.46% at 291 W fundamental power. Similar to the former dual-segment device, the effective area is increased to 300 μm^2 for each segment to account for the spatial overlap of the particular LiQPM grating and the fundamental wave. For the numerical integration of Eqs. (1) and (2), we used the absorption coefficients of the gratings and waveguides, as they have been measured separately (see Section 3.B). The final free parameter, which determines the effective nonlinearity in each grating, is the modulation depth v. For each channel, the modulation depth v is fitted to match the measured power of the SH. The modulation depths v range between 0.866 and 0.902, and good agreement of the measured temperature acceptance width as well as SH power is obtained. The peak at 130°C is larger than predicted by theory, i.e., it is larger than the side lobe of the 6.6 μm grating. One reason for this might be that some part of grating B exhibits a period that is increased by about 20 nm.

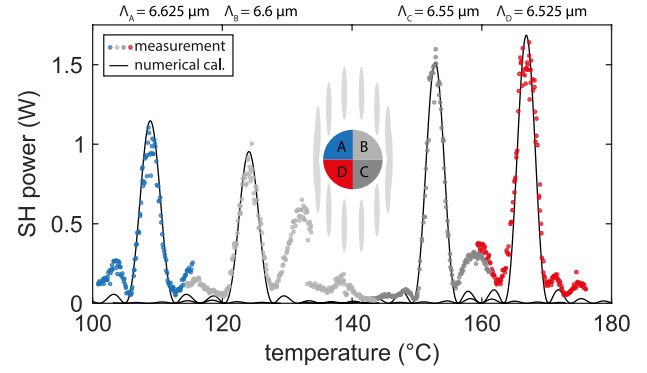The significance of the presented four-segment LiQPM device is twofold. On one hand, the spatial overlap of the fundamental wave and a particular grating segment is intrinsically reduced, which in turn limits the maximum efficiency. This, however, is counterbalanced by the fact that dense packaging of multi-wavelength frequency conversion elements becomes possible. On the other hand, the presented four-segment LiQPM structure identifies the first experimental realization of a 3D QPM device integrated in a waveguide. Whereas the former dual-segment LiQPM structure could, in principle, also be fabricated using a specifically poled crystal, any kind of non-uniform $\chi^{(2)}$ modification along the crystallographic c axis, as is the case for the A-D and B-C segments, is not possible by classic fabrication methods but becomes available using LiQPM. The 3D capability of LiQPM can be extended to more sophisticated applications such as nonlinear beam shaping.

D. Helically Twisted Structure for Nonlinear Beam Shaping

Finally, we propose a concept for the nonlinear generation of optical vortex beams by a helically twisted nonlinear susceptibility. As illustrated in Fig. 10(a), the $\chi^{(2)}$ modulation circuits around the optical axis in longitudinal direction with a period that fulfills the QPM condition for SHG. As a first experimental proof of principle, we want to show the fabrication of a helical nonlinear structure and its properties. Therefore, larger structures with a transverse diameter of 35 μm to 50 μm and a length of 6 mm have been induced first without waveguides. These structures can be better analyzed microscopically. The resolution of the setup allows us to inscribe helical structures with a diameter of 12 μm into waveguides. However, the waveguide has to support guiding of the shaped SH mode. To accomplish this, the waveguide parameters have to be adapted accordingly. Magnesium doped x-cut lithium niobate substrates are employed as a host material to account for threshold characteristics and focus splitting that occur for large-scale structures using z-cut samples [41,42]. According to the dopant concentration and associated change in dispersion, an increased QPM period of 6.7 μm is selected [43]. Similar to the 3D schematic [Fig. 10(a)], the 3D SHG microscope image reveals the twisted nature of the 3D pattern [Fig. 10(b)]. A projection of the realized structure is shown in Fig. 11(b). The bended periods are clearly visible. The detected SH signal as a function of the temperature is shown in Fig. 11(c) where a fundamental pulse energy of 2 μJ is employed. A phase-matching temperature of approximately
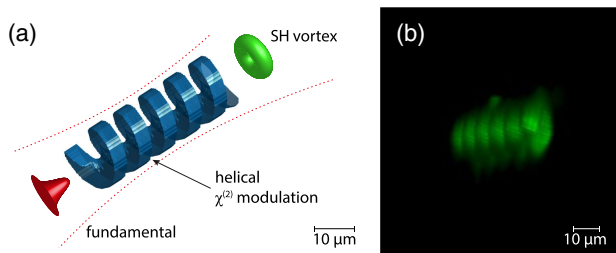
Fig. 10. SHG with helical twisted structure. (a) Illustration of a helical LiQPM grating that transfers a fundamental Gaussian beam into a vortex second-harmonic beam. (b) 3D view of SHG microscope images of the helical LiQPM grating fabricated in magnesium doped *x*-cut lithium niobate (see Visualization 1).
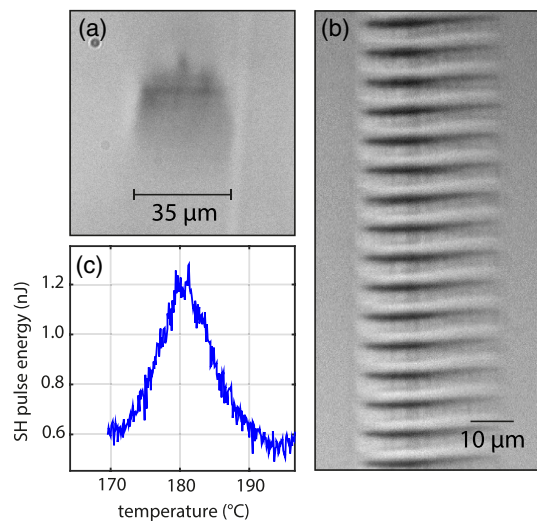

Fig. 11. Microscope images and SH power. (a) Microscope image of the front face of a large-scale helical QPM structure. (b) Microscope image from the top where the bended periods of the helical structure are visible. (c) Temperature tuning of SH power.

180°C is obtained for the volume structured material and extraordinary polarization. In this demonstration, the fabricated device provides limited homogeneity along the vertical direction, which is best seen in the microscope image of the front face of the helical structure [Fig. 11(a)]. Thus, the non-uniform conversion strength made it impossible to record the characteristic vortex pattern in this first experimental approach. One reason for the inhomogeneities is that the pulse energy drifts slightly over the long fabrication time of 36 h. The fabrication time will be reduced by two orders of magnitude if a pulse laser with a repetition rate of 100 kHz would be used. The second reason is the large refractive index of lithium niobate that leads to spherical aberrations. Spherical aberrations have to be compensated for in future experiments, for instance, by using a spatial light modulator [44].

5. CONCLUSION

We have demonstrated monolithic fabrication of waveguides with integrated 3D nonlinear photonic structures by LiQPM. The integration of 3D QPM structures into waveguides increases the conversion efficiency compared to nonlinear photonic crystals. Depressed-cladding waveguides with almost single-mode

guiding and reasonable loss are fabricated by carefully choosing pulse energy and writing velocity. These parameters were optimized as well for the LiQPM structures to get the highest possible SHG power. We have fabricated chirped structures for broadband SHG as well as cascaded single-period structures for multi-wavelength SHG. As LiQPM allows for the fabrication of periods down to 2 µm, structures for SHG of 800 nm fs-laser pulses can be designed. Parallel multi-wavelength frequency conversion becomes possible by splitting the waveguide core into two or four parts, allowing for compact designs. Especially the quad-core structure cannot be realized by electric field poling. It is the first experimental demonstration of the integration of a 3D QPM structure into a waveguide. The proposed concept of a helically twisted nonlinear photonic structure for SH vortex generation shows the potential for nonlinear beam-shaping devices. Our results open new avenues for creating ultra-compact devices for advanced QPM.

REFERENCES

1. J. A. Armstrong, N. Bloembergen, J. Ducuing, and P. S. Pershan, "Interactions between light waves in a nonlinear dielectric," Phys. Rev. **127**, 1918–1939 (1962).
2. M. M. Fejer, G. A. Magel, D. H. Jundt, and R. L. Byer, "Quasi-phase-matched second harmonic generation: tuning and tolerances," IEEE J. Quantum. Electron. **28**, 2631–2654 (1992).
3. B. Chen, C. Xu, B. Zhou, and X. Tang, "Analysis of cascaded second-order nonlinear interaction based on quasi-phase-matched optical waveguides," IEEE J. Sel. Top. Quantum Electron. **8**, 675–680 (2002).
4. C.-Q. Xu and B. Chen, "Cascaded wavelength conversions based on sum-frequency generation and difference-frequency generation," Opt. Lett. **29**, 292–294 (2004).
5. M. F. Saleh, G. Di Giuseppe, B. E. A. Saleh, and M. C. Teich, "Photonic circuits for generating modal, spectral, and polarization entanglement," IEEE Photon. J. **2**, 736–752 (2010).
6. S. Tanzilli, A. Martin, F. Kaiser, M. De Micheli, O. Alibart, and D. Ostrowsky, "On the genesis and evolution of integrated quantum optics," Laser Photon. Rev. **6**, 115–143 (2012).
7. M. Houe and P. D. Townsend, "An introduction to methods of periodic poling for second-harmonic generation," J. Phys. D **28**, 1747–1763 (1995).
8. V. Berger, "Nonlinear photonic crystals," Phys. Rev. Lett. **81**, 4136–4139 (1998).
9. N. G. R. Broderick, G. W. Ross, H. L. Offerhaus, D. J. Richardson, and D. C. Hanna, "Hexagonally poled lithium niobate: a two-dimensional nonlinear photonic crystal," Phys. Rev. Lett. **84**, 4345–4348 (2000).
10. A. Arie and N. Voloch, "Periodic, quasi-periodic, and random quadratic nonlinear photonic crystals," Laser Photon. Rev. **4**, 355–373 (2010).
11. M. Ayoub, J. Imbrock, and C. Denz, "Second harmonic generation in multi-domain $\chi2$ media: from disorder to order," Opt. Express **19**, 11340–11354 (2011).
12. X. Chen, P. Karpinski, V. Shvedov, K. Koynov, B. Wang, J. Trull, C. Cojocaru, W. Krolikowski, and Y. Sheng, "Ferroelectric domain engineering by focused infrared femtosecond pulses," Appl. Phys. Lett. **107**, 141102 (2015).
13. X. Chen, P. Karpinski, V. Shvedov, A. Boes, A. Mitchell, W. Krolikowski, and Y. Sheng, "Quasi-phase matching via femtosecond laser-induced domain inversion in lithium niobate waveguides," Opt. Lett. **41**, 2410–2413 (2016).
14. J. Thomas, V. Hilbert, R. Geiss, T. Pertsch, A. Tünnermann, and S. Nolte, "Quasi phase matching in femtosecond pulse volume structured x-cut lithium niobate," Laser Photon. Rev. **7**, L17–L20 (2013).
15. J. Imbrock, H. Hanafi, M. Ayoub, and C. Denz, "Local domain inversion in MgO-doped lithium niobate by pyroelectric field-assisted femtosecond laser lithography," Appl. Phys. Lett. **113**, 252901 (2018).

16. D. Wei, C. Wang, H. Wang, X. Hu, D. Wei, X. Fang, Y. Zhang, D. Wu, Y. Hu, J. Li, S. Zhu, and M. Xiao, "Experimental demonstration of a three-dimensional lithium niobate nonlinear photonic crystal," Nat. Photonics **12**, 596–600 (2018).

17. T. Xu, K. Switkowski, X. Chen, S. Liu, K. Koynov, H. Yu, H. Zhang, J. Wang, Y. Sheng, and W. Krolikowski, "Three-dimensional nonlinear photonic crystal in ferroelectric barium calcium titanate," Nat. Photonics **12**, 591–595 (2018).

18. S. Liu, K. Switkowski, C. Xu, J. Tian, B. Wang, P. Lu, W. Krolikowski, and Y. Sheng, "Nonlinear wavefront shaping with optically induced three-dimensional nonlinear photonic crystals," Nat. Commun. **10**, 3208 (2019).

19. D. Wei, C. Wang, X. Xu, H. Wang, Y. Hu, P. Chen, J. Li, Y. Zhu, C. Xin, X. Hu, Y. Zhang, D. Wu, J. Chu, S. Zhu, and M. Xiao, "Efficient nonlinear beam shaping in three-dimensional lithium niobate nonlinear photonic crystals," Nat. Commun. **10**, 4193 (2019).

20. M. Yamada, N. Nada, M. Saitoh, and K. Watanabe, "First-order quasi-phase matched LiNbO₃ waveguide periodically poled by applying an external field for efficient blue second-harmonic generation," Appl. Phys. Lett. **62**, 435–436 (1993).

21. Y. L. Lee, N. E. Yu, C. Jung, B. A. Yu, I. B. Sohn, S. C. Choi, Y. C. Noh, D. K. Ko, W. S. Yang, H. M. Lee, W. K. Kim, and H. Y. Lee, "Second-harmonic generation in periodically poled lithium niobate waveguides fabricated by femtosecond laser pulses," Appl. Phys. Lett. **89**, 171103 (2006).

22. R. Osellame, M. Lobino, N. Chiodo, M. Marangoni, G. Cerullo, R. Ramponi, H. T. Bookey, R. R. Thomson, N. D. Psaila, and A. K. Kar, "Femtosecond laser writing of waveguides in periodically poled lithium niobate preserving the nonlinear coefficient," Appl. Phys. Lett. **90**, 241107 (2007).

23. J. Thomas, M. Heinrich, J. Burghoff, S. Nolte, A. Ancona, and A. Tünnermann, "Femtosecond laser-written quasi-phase-matched waveguides in lithium niobate," Appl. Phys. Lett. **91**, 151108 (2007).

24. S. Zhang, J. Yao, Q. Shi, Y. Liu, W. Liu, Z. Huang, F. Lu, and E. Li, "Fabrication and characterization of periodically poled lithium niobate waveguide using femtosecond laser pulses," Appl. Phys. Lett. **92**, 2006–2009 (2008).

25. Z. Huang, C. Tu, S. Zhang, Y. Li, F. Lu, Y. Fan, and E. Li, "Femtosecond second-harmonic generation in periodically poled lithium niobate waveguides written by femtosecond laser pulses," Opt. Lett. **35**, 877–879 (2010).

26. F. Chen and J. R. V. de Aldana, "Optical waveguides in crystalline dielectric materials produced by femtosecond-laser micromachining," Laser Photon. Rev. **8**, 251–275 (2014).

27. S. Kroesen, K. Tekce, J. Imbrock, and C. Denz, "Monolithic fabrication of quasi phase-matched waveguides by femtosecond laser structuring the $\chi^{(2)}$ nonlinearity," Appl. Phys. Lett. **107**, 101109 (2015).

28. A. Bahabad and A. Arie, "Generation of optical vortex beams by nonlinear wave mixing," Opt. Express **15**, 17619–17624 (2007).

29. L. Tian, F. Ye, and X. Chen, "Optical vortex converter with helical-periodically poled ferroelectric crystal," Opt. Express **19**, 11591–11596 (2011).

30. N. V. Bloch, K. Shemer, A. Shapira, R. Shiloh, I. Juwiler, and A. Arie, "Twisting light by nonlinear photonic crystals," Phys. Rev. Lett. **108**, 233902 (2012).

31. K. Shemer, N. Voloch-Bloch, A. Shapira, A. Libster, I. Juwiler, and A. Arie, "Azimuthal and radial shaping of vortex beams generated in twisted nonlinear photonic crystals," Opt. Lett. **38**, 5470–5473 (2013).

32. B. Yang, X.-H. Hong, R.-E. Lu, Y.-Y. Yue, C. Zhang, Y.-Q. Qin, and Y.-Y. Zhu, "2D wave-front shaping in optical superlattices using nonlinear volume holography," Opt. Lett. **41**, 2927–2929 (2016).

33. D. Wei, Y. Zhu, W. Zhong, G. Cui, H. Wang, Y. He, Y. Zhang, Y. Lu, and M. Xiao, "Directly generating orbital angular momentum in second-harmonic waves with a spirally poled nonlinear photonic crystal," Appl. Phys. Lett. **110**, 261104 (2017).

34. S. Kroesen, W. Horn, J. Imbrock, and C. Denz, "Electro-optical tunable waveguide embedded multiscan Bragg gratings in lithium niobate by direct femtosecond laser writing," Opt. Express **22**, 23339–23348 (2014).

35. Y. Sheng, A. Best, H.-J. Butt, W. Krolikowski, A. Arie, and K. Koynov, "Three-dimensional ferroelectric domain visualization by Čerenkov-type second harmonic generation," Opt. Express **18**, 16539–16545 (2010).

36. M. Ayoub, H. Futterlieb, J. Imbrock, and C. Denz, "3D imaging of ferroelectric kinetics during electrically driven switching," Adv. Mater. **29**, 1603325 (2017).

37. M. A. Arbore, A. Galvanauskas, D. Harter, M. H. Chou, and M. M. Fejer, "Engineerable compression of ultrashort pulses by use of second-harmonic generation in chirped-period-poled lithium niobate," Opt. Lett. **22**, 1341–1343 (1997).

38. M. A. Arbore, O. Marco, and M. M. Fejer, "Pulse compression during second-harmonic generation in aperiodic quasi-phase-matching gratings," Opt. Lett. **22**, 865–867 (1997).

39. G. Imeshev, M. A. Arbore, M. M. Fejer, A. Galvanauskas, M. Fermann, and D. Harter, "Ultrashort-pulse second-harmonic generation with longitudinally nonuniform quasi-phase-matching gratings: pulse compression and shaping," J. Opt. Soc. Am. B **17**, 304–318 (2000).

40. D. H. Jundt, "Temperature-dependent Sellmeier equation for the index of refraction, n_e, in congruent lithium niobate," Opt. Lett. **22**, 1553–1555 (1997).

41. G. Zhou, A. Jesacher, M. Booth, T. Wilson, A. Ródenas, D. Jaque, and M. Gu, "Axial birefringence induced focus splitting in lithium niobate," Opt. Express **17**, 17970–17975 (2009).

42. P. Karpinski, V. Shvedov, W. Krolikowski, and C. Hnatovsky, "Laser-writing inside uniaxially birefringent crystals: fine morphology of ultrashort pulse-induced changes in lithium niobate," Opt. Express **24**, 7456–7476 (2016).

43. N. Umemura, D. Matsuda, T. Mizuno, and K. Kato, "Sellmeier and thermo-optic dispersion formulas for the extraordinary ray of 5 mol % MgO-doped congruent LiNbO₃ in the visible, infrared, and terahertz regions," Appl. Opt. **53**, 5726–5732 (2014).

44. B. P. Cumming, A. Jesacher, M. J. Booth, T. Wilson, and M. Gu, "Adaptive aberration compensation for three-dimensional microfabrication of photonic crystals in lithium niobate," Opt. Express **19**, 9419–9425 (2011).